

Explicit-time Floquet topological superconductivity in a microwave/infrared frequency AC voltage-driven Josephson junction

Donghao Wang¹, Zixuan Ding¹, Mengyao Li², Yongchun Tao^{1,*} and Hao Fu^{3,†}

¹Department of Physics, Nanjing Normal University, Nanjing 210023, Jiangsu, China

²College of Science, Nanjing Forestry University, Nanjing 210037, Jiangsu, China

³School of Mathematical Sciences, Nanjing Normal University, Nanjing 210023, Jiangsu, China



(Received 10 October 2023; accepted 19 March 2024; published 16 April 2024)

Anomalous Floquet topological superconductivity with chirality can be achieved by applying a dc-bias voltage across the Josephson junction with a sandwiched magnetic topological insulator (TI), in which the intrinsic Josephson phase provides a time-dependent periodic driving [R.-X. Zhang and S. Das Sarma, *Phys. Rev. Lett.* **127**, 067001 (2021)]. In this work, we remove the bias voltage and connect the magnetic TI to an external AC voltage source to modulate the chemical potential, thus bringing about an explicit-time Floquet periodic driving. In the context of the driving, the system is similarly found to convert into a two-dimensional anomalous Floquet topological superconductor with chirality. By tuning the AC voltage source's frequency, we obtain a rich variety of novel Floquet topological superconducting phases with chirality. Particularly, by manipulating such static parameters as Zeeman field and superconducting pairing potential, a series of topological superconducting phase transitions are also exhibited, accompanied by exotic Floquet topological superconducting phases with chirality.

DOI: [10.1103/PhysRevResearch.6.023059](https://doi.org/10.1103/PhysRevResearch.6.023059)

I. INTRODUCTION

In recent years, several distinguished topological phases have attracted great attention, such as Chern insulators [1–3], topological insulators (TIs) [4–9], and topological superconductors (TSCs) [10–13]. More importantly, there is an intrinsic connection between non-Abelian Majorana zero modes and TSCs, which builds a bridge between condensed matter physics and quantum computation [14–19].

An interesting observation is that quantum systems also reveal topological properties when experiencing periodic driving beyond the adiabatic regime. The driving was initially expected to trigger topological phase transitions [20–22], but can also generate specific topological properties, which are incomprehensible in the classical framework of topological band theory [23,24]. In such periodic driving systems, the induced topological phases are governed by the Floquet theory [23,25–31] and have aroused interest significantly in experiments. Several artificial systems have been suggested to investigate analogous phases, such as one-dimensional (1D) quantum walks with photons [32] and two-dimensional (2D) waveguide lattices [33].

However, few studies have been reported on the corresponding superconducting counterpart except for only one

recent theoretical work, in which a 2D anomalous Floquet chiral topological superconducting Josephson junction was proposed [34]. The Floquet topological superconducting physics with the chiral Majorana edge modes (MEMs) is considered to stem entirely from the intrinsic dynamics due to the dc-bias Josephson effect.

In contrast to this intrinsic driving, an explicit time-dependent period driving was obtained through a microwave voltage source (modulation of the chemical potential), which was inflicted on a planar Josephson junction with a 2D electron gas separating two superconducting leads. Both Majorana zero and π modes were found to co-occur accompanied by subharmonic response, which affords the possibility to unequivocally identify Majorana modes [35].

On the other hand, the chemical potential μ , Zeeman field g_z , and proximity-induced superconducting energy gap $\Delta_{I(b)}$ can exert a great influence on the generation of topological phases, as demonstrated in a variety of materials with low and three dimensions. For a nonuniform 1D p -wave superconducting wire with a periodically modulated μ , the fate of the Majorana fermions (MFs) was investigated under the density modulation and disorder [36]. The modulated potential μ is of benefit to the formation of periodic density waves and the topological superconducting phase could be destroyed for the large modulation amplitude. g_z applied to semiconductor quantum wires with strong spin-orbit coupling and in contact with s -wave superconductors (SCs) was also studied. A topological phase, which supports end Majorana fermions and offers an enticing platform for implementing topological quantum information processing, can be achieved [37].

Then, a natural question is raised whether both the explicit time-dependent periodic driving and adjustment of the static parameters g_z and $\Delta_{I(b)}$ are significant for generating the

*yctao88@163.com

†haofu@njnu.edu.cn

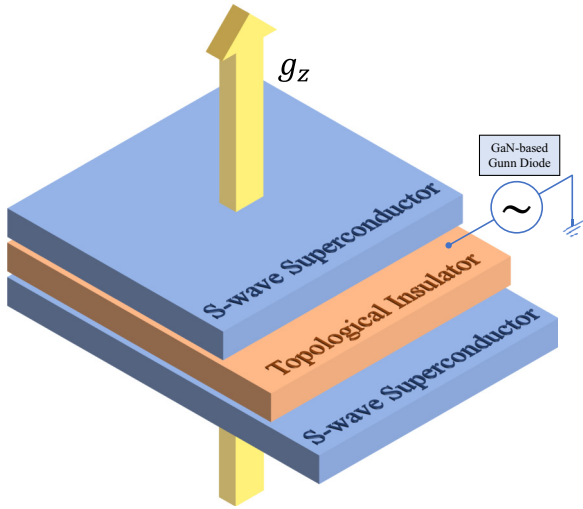


FIG. 1. Schematic diagram of a Floquet TSC Josephson hybrid structure, which consists of top and bottom s -wave SCs and a sandwiched thin layer of TI. A Zeeman field g_z is applied along the z direction and a microwave/infrared frequency AC voltage source (e.g., GaN-based Gunn diodes) is connected to the interface of the magnetic TI thin layer and SC, leading to the chemical potential μ as a periodic modulation.

Floquet chiral topological superconducting phase or not. To the best of our knowledge, the systematic study is of extreme paucity, which is urgently demanded and also the main incentive of this work.

In this work, we construct a Josephson hybrid structure with a sandwiched magnetic TI, which is subject to a Zeeman field g_z and connected to an AC voltage source, as shown in Fig. 1. Here, the explicit-time periodic driving brought by the AC voltage source makes the whole system evolve into a 2D anomalous Floquet chiral TSC.

Our structure differs markedly from that in Ref. [34]. The standard Josephson junction operation induces an intrinsically implicit time-periodic phase due to the bias voltage between the two superconducting layers in Ref. [34], seen in the Hamiltonian's off-diagonal elements. We remove the bias voltage and use an AC voltage source coupled to the TI instead. This explicit-time operation makes the Hamiltonian's diagonal elements, which refer to the chemical potential, oscillate periodically with time [see Eq. (5)]. Hence the explicit and implicit time dependencies and their effects on different materials lead to different Hamiltonians and topological properties. Analogously, a lot of anomalous Floquet topological superconducting phases appear in our structure as shown below.

We find that, at a small \mathcal{T} of the AC voltage source, the system is within the high-frequency ω limit ($\mathcal{T} = 2\pi/\omega$) and its topological properties resemble those of the traditional static TSC, namely, the number of edge states matches the bulk band Chern number. However, the system will cross the high-frequency limit as \mathcal{T} is gradually raised, generating a series of novel anomalous Floquet superconducting topological phases and the corresponding topological phase transitions. These anomalous Floquet topological phases require both the Chern number and the winding number to be characterized, which

have a different bulk-edge correspondence relation from the conventional static topological superconducting phase. We obtain the number of edge states by the local density of states (LDOS) distribution and numerically calculate the winding number and BdG Chern number to verify the new bulk-edge correspondence relation. Meanwhile, we present a detailed demonstration of two types of topological phase transitions, one triggered by the variation of \mathcal{T} and the other by the alteration of the static parameters under a fixed \mathcal{T} .

The rest of this paper is organized as follows. In Sec. II, we introduce the model with its BdG Hamiltonian and Floquet Hamiltonian. The theoretical and computational methods utilized are also shown. The phase diagram of the anomalous Floquet topological superconducting phase is shown in Sec. III, where we employ the bulk bands to analyze the phase transition origins and provide the edge states by using the LDOS method. In Sec. IV, we give a brief discussion of experimental feasibility, covering the fabrication of Josephson junction structure, the probable effects of AC voltage source heating, and the experimental examination of edge states. Finally, the summary and outlook are given in Sec. V.

II. MODEL HAMILTONIAN AND FLOQUET THEORY

A. Model Hamiltonian

Without losing generality, we define the tight-binding model Hamiltonian on a square lattice. The four-band Hamiltonian of TI thin film can be represented as [38–41]

$$\begin{aligned} \hat{H}_0 &= \sum_{\mathbf{k}} \hat{\psi}_{\mathbf{k}}^\dagger H_0(\mathbf{k}) \hat{\psi}_{\mathbf{k}}, \\ H_0(\mathbf{k}) &= t(\mathbf{k})\tau_x \otimes \mathbf{I}_{2 \times 2} + \hbar v \left(\sin k_x \tau_z \otimes \sigma_y \right. \\ &\quad \left. - \sin k_y \tau_z \otimes \sigma_x \right) + g_z \mathbf{I}_{2 \times 2} \otimes \sigma_z, \end{aligned} \quad (1)$$

with the basis vector $\hat{\psi}_{\mathbf{k}} = [c_{1\mathbf{k}\uparrow}, c_{1\mathbf{k}\downarrow}, c_{2\mathbf{k}\uparrow}, c_{1\mathbf{k}\downarrow}]^T$, in which 1(2) represents the TI's top(bottom) surface or the TI-SC interface and \uparrow (\downarrow) denotes spin up(down). Here, $t(\mathbf{k}) = t_0 - t_1(\cos k_x + \cos k_y)$ refers to the hybridization of the top and bottom surfaces, v is the Fermi velocity, \hbar is the reduced Planck constant, and $g_z \mathbf{I}_{2 \times 2} \otimes \sigma_z$ stands for the Zeeman splitting term caused by the magnetic field in the z direction. The Pauli matrices σ_i indicate the spin and τ_i the opposite surfaces of the TI.

The superconducting proximity effect of the opposite surfaces can be incorporated in the BdG Hamiltonian

$$\begin{aligned} \hat{H}_{\text{BdG}} &= \sum_{\mathbf{k}} \hat{\Psi}_{\mathbf{k}}^\dagger H_{\text{BdG}}(\mathbf{k}) \hat{\Psi}_{\mathbf{k}}, \\ H_{\text{BdG}}(\mathbf{k}) &= \begin{pmatrix} H_0(\mathbf{k}) - \mu & \Delta \\ \Delta^\dagger & -H_0^T(-\mathbf{k}) + \mu \end{pmatrix}, \end{aligned} \quad (2)$$

with the basis vector

$$\hat{\Psi}_{\mathbf{k}} = [c_{1\mathbf{k}\uparrow}, c_{1\mathbf{k}\downarrow}, c_{2\mathbf{k}\uparrow}, c_{1\mathbf{k}\downarrow}, c_{1\mathbf{k}\uparrow}^*, c_{1\mathbf{k}\downarrow}^*, c_{2\mathbf{k}\uparrow}^*, c_{1\mathbf{k}\downarrow}^*]^T, \quad (3)$$

where the s -wave superconducting pairing potential Δ has the following specific form:

$$\Delta = \begin{pmatrix} -i\Delta_t \sigma_y & 0 \\ 0 & -i\Delta_b \sigma_y \end{pmatrix}, \quad (4)$$

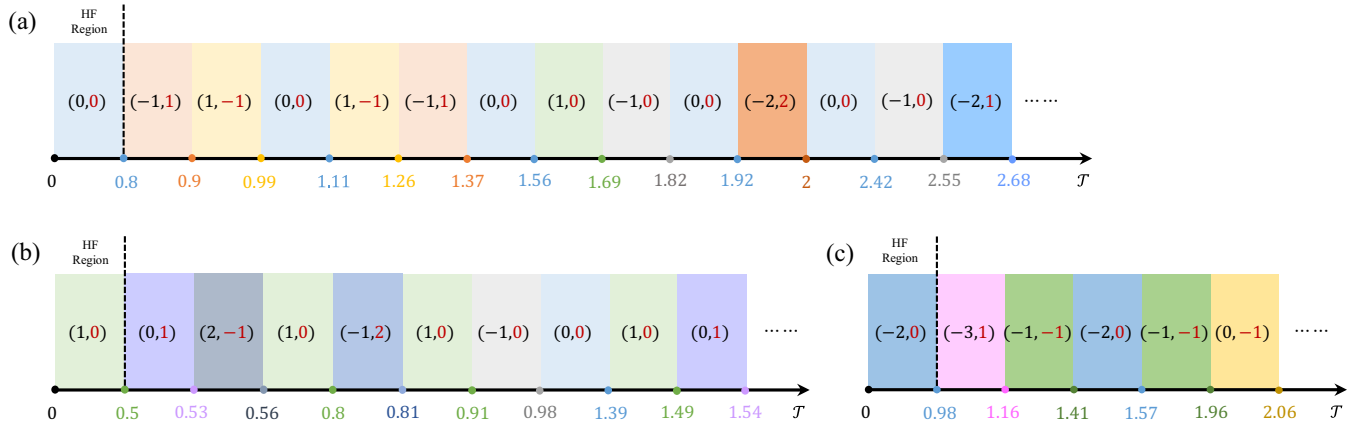


FIG. 2. Topological phase diagram under the periodic driving \mathcal{T} , where the topological phase is represented by the integer topological invariants Chern number and winding number, written as $(\mathcal{C}, \mathcal{W})$ in the table. The first topological phase region in each subplot is the high-frequency one that we define and its boundary is clearly shown by the black dashed line. Three sets of different parameter settings are chosen as $\mu = 1$, $\Delta_b = 0.4$, (a) $g_z = 0.6$, $\Delta_t = 2.4$, (b) $g_z = 2.87$, $\Delta_t = 2.4$, and (c) $g_z = 0.6$, $\Delta_t = 0.8$.

with Δ_t and Δ_b the superconducting pairing potentials of the opposite surfaces, respectively, and μ refers to the chemical potential of the TI.

The time period we consider is driven by periodic oscillations of the chemical potential, resulting from a microwave/infrared frequency AC voltage source that is coupled to the TI. It is written as $\mu(t) = \mu[1 + \cos(\omega t)]$ with the frequency of the AC voltage source $\omega = 2\pi/\mathcal{T}$. Then, the time-dependent BdG Hamiltonian of the system is given by

$$H(\mathbf{k}, t) = \begin{pmatrix} H_0(\mathbf{k}) - \mu(t) & \Delta \\ \Delta^\dagger & -H_0^T(-\mathbf{k}) + \mu(t) \end{pmatrix}. \quad (5)$$

The periodic driving converts the static TSC Josephson junction into a Floquet TSC one, which enables us to utilize the Floquet-Bloch theory and derive the matrix elements of the Floquet Hamiltonian in the extended Hilbert space [42]

$$(H_F)_{nm} = h_\omega^{n-m} + \omega n \delta_{nm}, \quad n, m \in \mathbb{Z}. \quad (6)$$

Here, $h_\omega^{n-m} = 1/\mathcal{T} \int_0^\mathcal{T} H(\mathbf{k}, t) e^{i(n-m)\omega t} dt$, from which the term of each order can be simply derived:

$$\begin{aligned} h_\omega^{(0)} &= H(\mathbf{k}, t)[\cos(\omega t) \rightarrow 0], \\ h_\omega^{(1)} &= -\frac{\mu}{2} \left(\sigma_z \otimes \mathbf{I}_{4 \times 4} \right), \end{aligned} \quad (7)$$

with $h_\omega^{(-1)} = (h_\omega^{(1)})^\dagger$. Thus the infinite-dimensional form of the Floquet Hamiltonian can be written as

$$H_F = \begin{bmatrix} \ddots & \vdots & \vdots & \vdots & \ddots \\ \dots & h_\omega^{(0)} - \omega & h_\omega^{(1)} & h_\omega^{(2)} & \dots \\ \dots & h_\omega^{(-1)} & h_\omega^{(0)} & h_\omega^{(1)} & \dots \\ \dots & h_\omega^{(-2)} & h_\omega^{(-1)} & h_\omega^{(0)} + \omega & \dots \\ \ddots & \vdots & \vdots & \vdots & \ddots \end{bmatrix}. \quad (8)$$

For the matrix elements with $|n-m| > 1$, Eq. (6) indicates that $(H_F)_{nm} = 0$. We take a truncation of the infinite-dimensional matrix to $m, n = 5$ in Eq. (8), which can ensure

sufficient numerical accuracy and convergence with a reasonable computational complexity.

Next, by using the Magnus Expansion, the effective Hamiltonian H_{eff} of the system can be derived as [43,44]

$$H_{\text{eff}} = H_{\text{ME}} = H_{\text{ME}}^{(0)} + \frac{1}{\omega} H_{\text{ME}}^{(1)} + \frac{1}{\omega^2} H_{\text{ME}}^{(2)} + \dots, \quad (9)$$

where

$$\begin{aligned} H_{\text{ME}}^{(0)} &= \frac{1}{\mathcal{T}} \int_0^\mathcal{T} dt H(t), \\ H_{\text{ME}}^{(1)} &= \sum_{n=1}^{\infty} \frac{1}{n} ([H_n, H_{-n}] \\ &\quad - e^{in\omega t} [H_n, H_0] + e^{-in\omega t} [H_{-n}, H_0]), \end{aligned} \quad (10)$$

with H_n the Fourier expansion of $H(t)$, specifically $H(t) = \sum_{n \in \mathbb{Z}} (H_n e^{in\omega t})$. The effective Hamiltonian approximately reduces to $H_{\text{eff}} \simeq H_{\text{ME}}^{(0)} = \frac{1}{\mathcal{T}} \int_0^\mathcal{T} dt H(t) = h_\omega^{(0)}$ in the high-frequency limit, which corresponds to the range where the system has not entered the anomalous Floquet TSC phase, as indicated in Fig. 2. Its topological properties resemble those of the traditional static TSC. Hence the time-dependent periodic driving problem becomes a static one. The periodic variation terms in the time-dependent Hamiltonian become zero in the high frequency. It is deduced that the zeroth-order term of the Floquet Hamiltonian H_F is essentially the same as the effective Hamiltonian in the high-frequency limit. This is due to the fact that the frequency ω is much higher than the energy band range of $h_\omega^{(0)}$ and the gap between the Floquet bulk energy bands is very large. Therefore, the topological properties of the system can be illustrated only by the zeroth-order term $h_\omega^{(0)}$ basically, which elucidates the reason why the system manifests similar topological properties to the traditional static TSC in the high-frequency limit. Here, it is worth pointing out that the analysis following Eq. (9) is limited to the high frequency range and cannot be used to obtain the full phase diagram as a function of the drive period \mathcal{T} .

B. Topological invariants

In order to identify the topological phase of the system, we need to calculate two topological invariants—the Chern number \mathcal{C} and the winding number \mathcal{W} . We use $(\mathcal{C}, \mathcal{W})$ to characterize the topological phase in the results and these two topological invariants also have corresponding relations with the edge states. To begin with, the BdG Chern number \mathcal{C} is defined on all the quasienergy bands lying between $[0, \omega/2]$ [45]

$$\mathcal{C} = \sum_n C_n, \quad (11)$$

where

$$C_n = \frac{1}{2\pi} \int_{BZ} d\mathbf{k}^2 \Omega_n(\mathbf{k}), \quad (12)$$

with the integral over the complete Brillouin zone and $\Omega_n(\mathbf{k})$ the Berry curvature, which can be further illustrated as a summation over the Floquet Hamiltonian eigenstates

$$\Omega_n(\mathbf{k}) = i \sum_{\alpha' \neq \alpha} \frac{\langle \psi_\alpha | \frac{\partial H_F}{\partial k_x} | \psi_{\alpha'} \rangle \langle \psi_{\alpha'} | \frac{\partial H_F}{\partial k_y} | \psi_\alpha \rangle - (k_x \leftrightarrow k_y)}{(\varepsilon_\alpha - \varepsilon_{\alpha'})^2}. \quad (13)$$

The above is the definition of the Chern number and, in the specific numerical computation, in order to simplify the calculation process, we use the following formula [24]:

$$C_n = \frac{i}{2\pi} \int_{BZ} dk_x dk_y \times \text{Tr}(P_n(k_x, k_y) [\partial_{k_x} P_n(k_x, k_y), \partial_{k_y} P_n(k_x, k_y)]), \quad (14)$$

with $P_n(k_x, k_y)$ the projection matrix given by the eigenvector of $H_F(k_x, k_y)$.

Here we obtain the BdG Chern number \mathcal{C} of the 2D anomalous Floquet chiral TSCs, which is completely different from that of the conventional Floquet chiral TSCs related to the Chern number. The latter is similar to the case in the high-frequency limit, which is adiabatically equivalent to the static chiral TSC.

Corresponding to the chiral MEMs in such a 2D anomalous Floquet chiral TSC, another relevant topological invariant, i.e., a homotopy-based winding number, is needed to deliberately describe them [23,24,27,46–48],

$$\mathcal{W} = \frac{1}{8\pi^2} \int_0^{\mathcal{T}} dt \iint_{BZ} d\mathbf{k} \text{Tr} \{ [U_\epsilon(\mathbf{k}, t)^{-1} \partial_t U_\epsilon(\mathbf{k}, t)] \times [[U_\epsilon(\mathbf{k}, t)^{-1} \partial_{k_x} U_\epsilon(\mathbf{k}, t)], [U_\epsilon(\mathbf{k}, t)^{-1} \partial_{k_y} U_\epsilon(\mathbf{k}, t)]] \}, \quad (15)$$

with $U_\epsilon(\mathbf{k}, t) = U(\mathbf{k}, t) [U(\mathbf{k}, \mathcal{T})]_\epsilon^{-\frac{t}{\mathcal{T}}}$, where the time-evolution unitary $U(\mathbf{k}, t) = \mathcal{T} \mathcal{O} \exp[-i \int_0^t H(\mathbf{k}, t) dt]$ with $\mathcal{T} \mathcal{O}$ denoting the time ordering and [49,50]

$$[U(\mathbf{k}, \mathcal{T})]_\epsilon^{-\frac{t}{\mathcal{T}}} = \sum_{m=1}^N \exp \left[-\frac{t}{\mathcal{T}} \log_{\epsilon_{\mathbf{k}}} (e^{-i\varepsilon_{m,\mathbf{k}}}) \right] P_{\mathbf{k},m}(\mathcal{T}), \quad (16)$$

with $P_{\mathbf{k},m}(\mathcal{T})$ the projection matrix given by the eigenvector of $U(\mathbf{k}, \mathcal{T})$ for $e^{-i\varepsilon_{m,\mathbf{k}}}$. Here $\epsilon_{\mathbf{k}}$ serves as the branch cut of the logarithm by requiring $i \log_{\epsilon_{\mathbf{k}}}(x) \in [\epsilon_{\mathbf{k}}, \epsilon_{\mathbf{k}} + 2\pi)$ for all

$x \in U(1)$. As we always set the branch cut to $\epsilon_{\mathbf{k}} = -\pi$, we have

$$i \log_{\epsilon_{\mathbf{k}}} (e^{-i\varepsilon_{m,\mathbf{k}}}) = \varepsilon_{m,\mathbf{k}}. \quad (17)$$

In numerical computation, the time-evolution unitary $U(\mathbf{k}, t)$ can be decomposed into [27,51]

$$U(\mathbf{k}, t) = \lim_{\Delta t \rightarrow 0} e^{-iH(\mathbf{k}, t - \Delta t)\Delta t} e^{-iH(\mathbf{k}, t - 2\Delta t)\Delta t} \dots \times e^{-iH(\mathbf{k}, \Delta t)\Delta t} e^{-iH(\mathbf{k}, 0)\Delta t}. \quad (18)$$

C. Quasi-one-dimensional Hamiltonian and boundary states from LDOS

In order to study the behavior of boundary states under quasi-one-dimensional geometric conditions, we consider the tight-binding representation of the Hamiltonian on a square lattice:

$$H = \sum_i \varphi_i^\dagger \begin{pmatrix} h_0 & \Delta \\ \Delta^\dagger & -h_0^T \end{pmatrix} \varphi_i + \sum_i \varphi_i^\dagger \begin{pmatrix} h_x & 0 \\ 0 & -h_x^T \end{pmatrix} \varphi_{i+\delta x} + \text{H.c.} + \sum_i \varphi_i^\dagger \begin{pmatrix} h_y & 0 \\ 0 & -h_y^T \end{pmatrix} \varphi_{i+\delta y} + \text{H.c.} \quad (19)$$

Here, i is the site index and $\delta x, \delta y$ represent unit vectors along the x and y directions respectively. The elements in the matrix are $h_0 = t_0(\sigma_x \otimes s_0) + g_z(\sigma_0 \otimes s_z) - \mu(\sigma_0 \otimes s_0)$, $h_x = \frac{1}{2}[-iv(\sigma_z \otimes s_y) - t_1(\sigma_x \otimes s_0)]$, and $h_y = \frac{1}{2}[-iv(\sigma_z \otimes s_x) - t_1(\sigma_x \otimes s_0)]$. We apply this Hamiltonian to a quasi-one-dimensional strip, considering the periodic boundary condition in the y direction, while taking the number of lattice points in the x direction as 100. In this case, k_y is a good quantum number and the system energy spectrum can be obtained by diagonalizing the Hamiltonian. Since we need to study the behavior of boundary states, we calculate the LDOS of the system, which is given by the following formula [52]:

$$\rho_i(k_y) = \frac{1}{2\pi} \text{Tr} [\text{Im} [G_i^R(k_y) - G_i^A(k_y)]], \quad (20)$$

$$G_i^R(k_y) = \sum_\alpha \frac{P_i(k_y)}{E - \varepsilon_\alpha(k_y) + i\eta},$$

with $G_i^R(k_y) = [G_i^A(k_y)]^\dagger$. In Eq. (20), $\varepsilon_\alpha(k_y)$ is the eigen-spectrum of the quasi-one-dimensional Floquet Hamiltonian, α represents the band index, the summation extends over all bands, and the projection operator $P_i(k_y) = |\psi_\alpha^i(k_y)\rangle \langle \psi_\alpha^i(k_y)|$. The distribution of the LDOS is exhibited at the boundary by a projecting operation, which can be interpreted as the probability distribution of the wave function on the i th strip in real space. Since the quasi-one-dimensional square lattice has 100 lattice points along the x direction, for the edge states, we take $i = 100$, and thus the corresponding probability is determined by $P_{100}(k_y)$.

III. RESULTS AND DISCUSSIONS

In this section, we investigate extensively how Floquet topological superconducting phases evolve with the tuning

of \mathcal{T} and diverse static parameters and also examine the association between the topological phase transitions and the band gap closure in different cases. Then, we verify the new bulk-edge correspondence relation by combining the topological invariants and number of edge states. In the calculation, the static parameters μ , $\Delta_{t(b)}$, and g_z are all measured in units of t_0 , which represents the hybridization energy or tunneling energy between the top and bottom surface states of the TI.

A series of rich Floquet topological superconducting phases are produced by tuning the driving period \mathcal{T} (in units of $1/t_0$) with the static parameters $\mu = 1$, $\Delta_t = 2.4$, $\Delta_b = 0.4$, and $g_z = 0.6$, which are characterized by both the Chern number and winding number as topological invariants [see Fig. 2(a)]. It is shown that the topological phase transitions are induced by the driving period \mathcal{T} , where seven different topological phases are displayed, namely $(0, 0)$, $(-1, 1)$, $(1, -1)$, $(1, 0)$, $(-1, 0)$, $(-2, 2)$, and $(-2, 1)$. The system remains in the high-frequency limit when the AC voltage source has a small driving period \mathcal{T} . In this case, there are no edge states near $E = \omega/2$, while the edge states at $E = 0$ match the Chern number, similar to the traditional static TSCs. As \mathcal{T} increases, the system starts to depart from the high-frequency region at 0.8 and undergoes a series of topological phase transitions, which are caused by the closing of the bulk bands at the high-symmetry points of the Brillouin zone at $E = \omega/2$ [see Fig. 3(a)]. Specifically, the dashed line in Fig. 3 corresponds to the energy $E = \omega/2$ and the occurrence of the topological phase transition is signified by the intersection of the high-symmetry points and the dashed line. This conforms to the essential theory of topology, namely, the gap closing is related to the occurrence of the topological phase transition and the alteration of the topological invariant [8]. The first four topological phase transitions in Fig. 2(a) are represented by the four dashed lines from the top to bottom in Fig. 3(a), respectively. The system transitions from the high-frequency region to the low-frequency one when the highest dashed line intersects with the high-symmetry point M at $\mathcal{T} = 0.8$. This corresponds to the first topological phase transition in Fig. 2(a). As \mathcal{T} increases, $\omega/2$ diminishes gradually and the high-symmetry point X is intersected by the second dashed line at $\mathcal{T} = 0.9$. This represents the second topological phase transition and so on. The similar correspondence is between Figs. 3(b) and 2(b).

With the Zeeman field strength g_z changed to 2.87, more new topological phases arise. The topological phase diagram is presented in Fig. 2(b) with the other parameters equal to those in Fig. 2(a). In contrast to Fig. 2(a), there exist three new Floquet topological superconducting phases, $(0, 1)$, $(2, -1)$, and $(-1, 2)$. All those topological phases, which have emerged in Fig. 2(a), have completely different driving periods. In addition, the same winding numbers are shared by the first four topological phases in Fig. 2(b) and those in Fig. 2(a), which is obvious from the sequence of the bulk band closing. Comparing Figs. 3(a) and 3(b), it is evident that the sequence of the first four closing points in both cases is M, X, Γ, M , and no edge states are occurring at $E = \omega/2$ in the high-frequency limit, so the winding numbers start from zero, which leads to the same winding number indices for the first four Floquet

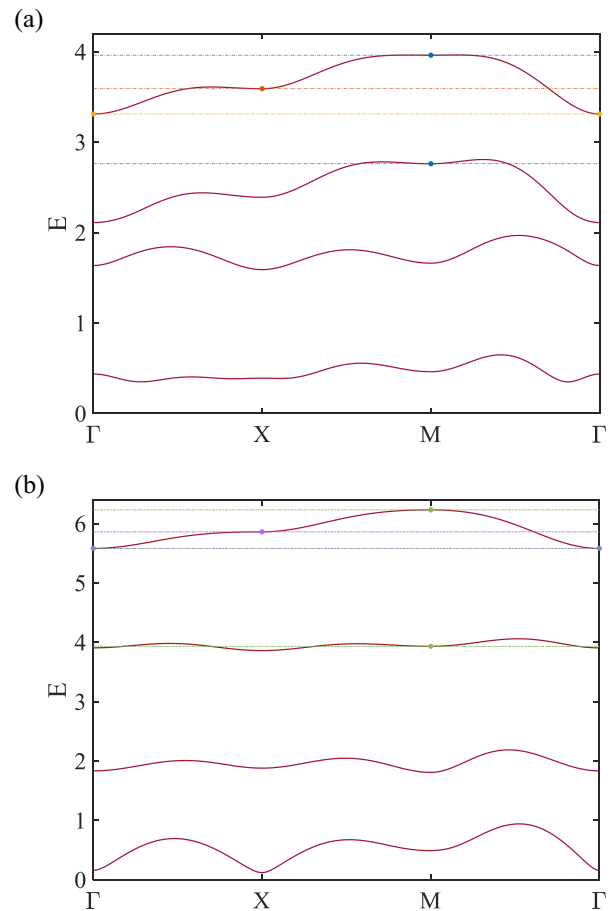


FIG. 3. Spectrum of bulk energy band in which the band gap closes at the Γ , X , and M points of the Brillouin zone sequentially. The dashed lines of different colors from the top to bottom indicate the energy $E = \omega/2$ of the band gap closing points. Here, $\mu = 1$, $\Delta_b = 0.4$, $\Delta_t = 2.4$, $g_z = 0.6$ for (a), and 2.87 for (b).

topological superconducting phases. From this, it can also be inferred that the interval of the topological phase transitions or the range of the existence of the topological phases is related to the distance between the high-symmetry points. For instance, as shown in Fig. 3(b), the distance between the third and fourth high-symmetry points is obviously larger than those between the first three adjacent high-symmetry points. This directly results in the second and third topological phases having a significantly narrower range than the fourth topological phase $(1, 0)$.

Similarly, using another set of parameters, where only Δ_t is changed to 0.8, many new topological phases can also be achieved, as illustrated in Fig. 2(c). Four completely novel topological phases, namely $(-2, 0)$, $(-3, 1)$, $(-1, -1)$, and $(0, -1)$, have not occurred in the prior two parameter choices. Similar to Fig. 2(b), the winding number indices of the first five topological phases in Fig. 2(c) are the same as those in Fig. 2(a), and their formation reasons resemble those explained in Fig. 2(b).

Under the three different sets of static parameters, a total of up to 14 different Floquet topological superconducting phases have occurred in the driving period modulation of \mathcal{T} .

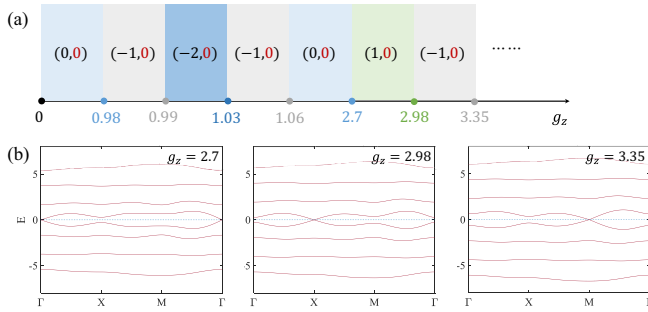


FIG. 4. (a) Topological phase diagram under the modulation of g_z at $\mathcal{T} = 0.1$ in the high-frequency region. Here $\mu = 1$, $\Delta_b = 0.4$, and $\Delta_t = 2.4$. (b) The variation of g_z causes the bulk energy band gap of the Floquet Hamiltonian to close at the Γ , X , and M points in the high-frequency region. Apart from g_z , the values of the other parameters are identical to those in (a).

In addition, the succession of the topological phases under the three sets of parameters are distinct from each other. The similar situations are for the corresponding topological phases under fixed \mathcal{T} . It follows that the explicit time-dependent periodic driving modulation under different static parameters induces various Floquet topological superconducting phases and topological phase transitions.

Moreover, the topological phase transitions are not only due to the closing of the bulk bands at the high-symmetry points of the Brillouin zone at $E = \omega/2$ but also the band gap closing at $E = 0$ can lead to the occurrence of topological phase transitions. In Fig. 4(a), we find a series of topological phase transitions occurring with the Zeeman field strength g_z . From Fig. 4(b), it can be seen that the bulk bands close at the Γ , X , and M points of the Brillouin zone, respectively, when $g_z = 2.7$, 2.98, and 3.35, which also lead to the emergence of topological phase transitions.

It is also worth noting that the topological properties of the system are completely different from those of the static TSC after the system exits the high-frequency limit region and the Chern number cannot fully capture the topological properties. Thus another topological invariant, namely the winding number, has to be introduced. As the driving period \mathcal{T} increases, the system gradually produces phase transitions from the high-frequency region to the low-frequency region. They are accompanied by the emergence of a series of anomalous Floquet topological superconducting phases, where the number of edge states does not conform to the conventional bulk-edge correspondence relation. The present bulk-edge correspondence relation is given by

$$n(0) = \mathcal{C} + \mathcal{W}, \quad n\left(\frac{\omega}{2}\right) = \mathcal{W}, \quad (21)$$

with the absolute value of $n(0)$ or $n(\omega/2)$ being the number of Majorana edge states at $E = 0$ or $\omega/2$ and the sign of n indicating the chirality of the edge states, where the negative (positive) values indicate the left- (right-) shifted chirality.

Now, taking the topological phases $(1, -1)$ and $(-1, 2)$ as examples, we explain the bulk-edge correspondence in detail. As shown in Fig. 5(a), the topological phase $(1, -1)$ has no edge states at $E = 0$, but its Chern number is not zero, and the number of edge states at $E = 0$ matches $\mathcal{C} + \mathcal{W} = 0$.

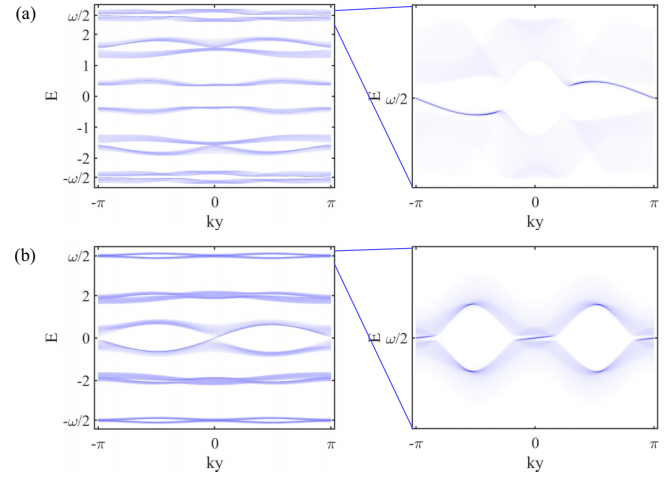


FIG. 5. Panels (a) and (b) are the edge state LDOS spectrum for the anomalous Floquet topological superconducting phases $(1, -1)$ and $(-1, 2)$, respectively. Here, $\mathcal{T} = 1.2$, $g_z = 0.6$ for the former and $\mathcal{T} = 0.81$, $g_z = 2.87$ for the latter; the other parameters are $\mu = 1$, $\Delta_b = 0.4$, and $\Delta_t = 2.4$.

Meanwhile, there is one left-shifted Majorana edge state near $E = \omega/2$, which matches $\mathcal{W} = -1$. Figure 5(b) shows the topological phase $(-1, 2)$, which has one right-shifted Majorana edge state near $E = 0$ and two right-shifted ones near $E = \omega/2$, perfectly satisfying Eq. (21).

IV. EXPERIMENTAL FEASIBILITY

In this section, we discuss the experimental feasibility of our proposed scheme. In the sandwich-hybrid structure of a thin layer of magnetic TI between two superconducting layers, Pb, Nb [53], or NbSe₂ [54] can be experimentally chosen as the SCs and (Bi, Sb)₂Se₃ [7,55–57] and Nb [58,59] thin films with Cr doping as the magnetic TI.

The magnitude of the hybridization energy t_0 is around meV, which can be tuned by varying the thickness of the TI layer [60].

The periodic driving is provided by a microwave/infrared frequency AC voltage source attached to the TI-SC interface. TIs are insulating in the bulk, but possess metallic surface states [8,52,61,62]; the contact of the AC voltage source on the surface can generate a periodic modulation of the chemical potential [35]. As long as the AC voltage source touches the surface, it can adjust the chemical potential of the interface state, indicating the contact does not act on the entire interface.

Considering the realistic energy scale, if NbSe₂ is used as the superconducting layer (superconducting gap of 0.5 meV), then the periodic driving frequency covers the range from microwave to infrared. Therefore, the microwave and terahertz frequency voltage sources are required in the low (below 300 GHz) and high (300 GHz \sim 1.5 THz) frequency ranges, respectively. We can employ Gunn diodes as these voltage sources, for example, GaN-based Gunn diodes [63], which operate adjustably in a frequency range of 100 GHz \sim 1.8 THz. And thus the demand of covering the microwave to infrared frequency range can be satisfied. Also, it should

be uncomplicated and straightforward to control other static parameters.

However, the microwave/infrared frequency AC voltage source can also cause thermal effects, which affect the Josephson current, the superconducting pairing potential $\Delta(T) = \Delta_0 \tanh(1.74\sqrt{T_c/T} - 1)$ [64], and the electron dephasing rate in the TI layer [65]. These effects can be mitigated by keeping the temperature as low as feasible or by modifying T_c and Δ_0 of the SC through doping, strain, electric field, and so on. As for detecting the edge states of the Floquet topological phase, we can use the scanning tunneling microscope (STM) to obtain the LDOS curves of the bulk and the boundary, which are similar to the dI/dV ones in Fig. 1 of Ref. [8]. Specifically, we need to place the STM probe at the edge of the TI. The dI/dV spectroscopy suggests the sharp peaks of the LDOS near 0 and $\omega/2$, which correspond to the chiral edge modes with 0 and $\omega/2$ gaps, respectively. Consequently, we hope that this explicit time-periodic driving topological superconducting Josephson junction structure based on microwave/infrared frequency AC voltage source modulation, and its rich Floquet topological properties, can be conformed in future experimental reports.

V. SUMMARY

To summarize, we have constructed a TSC Josephson junction, which is subjected to an explicit time-periodic driving based on a microwave/infrared frequency AC voltage source modulation, and revealed various novel anomalous Floquet chiral topological superconducting phases. In particular, we have observed that modifying the static parameters, such as Δ , and g_z , can trigger more exotic Floquet topological superconducting phase transitions. The features for the emergence of the topological superconducting phase transitions are as follows. (1) At fixed static parameters, the system steadily departs from the high-frequency region as the driving period \mathcal{T} of the AC voltage source enlarges or the frequency ω diminishes, resulting in many topological phase transitions and producing a series of novel anomalous Floquet topological superconducting phases. The origin of their appearance is the elimination of the energy gap at the high-symmetry point $E = \omega/2$ of the bulk bands. (2) At fixed \mathcal{T} , topological phase

transitions can also occur when tuning the static parameters, but these topological phase transitions are distinct from the former since they are induced by the closure of the bulk bands at $E = 0$. (3) For topological properties, \mathcal{T} being in the high-frequency region makes the topological phases resemble the conventional static topological superconducting phases. However, when \mathcal{T} departs from the high-frequency region, the topological phases turn into anomalous Floquet chiral phases of topological superconductivity, which demand both the winding number and the Chern number to illustrate them. The bulk-edge correspondence under the anomalous Floquet chiral topological superconducting phases is $n(0) = \mathcal{C} + \mathcal{W}$ with $n(\omega/2) = \mathcal{W}$.

Additionally, higher-order topological superconducting phases (HOTSP) in various dimensions have aroused abundant interest recently. Particularly, the Floquet HOTSPs have been predicted theoretically. For instance, 2D anomalous Floquet TSC might possess localized Majorana corner modes in the 0 and π gaps. They are tightly associated with the singularities in the phase spectrum of the system's bulk time-evolution operator [66–68]. Their numbers and locations depend on specific higher-order topological indices, which display different behaviors in systems with different symmetries. Moreover, the Majorana corner modes in 2D static systems are also influenced by different types of superconducting pairing potentials and geometric boundary shapes [69–71]. The edge theory is developed to theoretically explain not only the formation mechanism of Majorana corner modes but also 3D HOTSPs. It is noteworthy that the theory is also utilized in 2D and 3D Floquet counterparts [72,73]. Unfortunately, we have not attained localized Majorana corner modes in the present structure, which may originate from the fact that the edge state gap always closes [70]. Our future work will involve finding modulation methods to enable Floquet HOTSP in the current structure by the aid of the phase spectrum and edge theory methods.

ACKNOWLEDGMENTS

We thank Prof. R.-X. Zhang from the University of Tennessee, Knoxville for helpful discussion. This work was supported by the National Natural Science Foundation of China (Grant No. 12274232).

-
- [1] C.-X. Liu, S.-C. Zhang, and X.-L. Qi, The quantum anomalous Hall effect: Theory and experiment, *Annu. Rev. Condens. Matter Phys.* **7**, 301 (2016).
 - [2] F. D. M. Haldane, Model for a quantum Hall effect without Landau levels: Condensed-matter realization of the “parity anomaly”, *Phys. Rev. Lett.* **61**, 2015 (1988).
 - [3] G. Chen, A. L. Sharpe, E. J. Fox, Y.-H. Zhang, S. Wang, L. Jiang, B. Lyu, H. Li, K. Watanabe, T. Taniguchi, Z. Shi, T. Senthil, D. Goldhaber-Gordon, Y. Zhang, and F. Wang, Tunable correlated Chern insulator and ferromagnetism in a moiré superlattice, *Nature (London)* **579**, 56 (2020).
 - [4] C. L. Kane and E. J. Mele, Z_2 topological order and the quantum spin Hall effect, *Phys. Rev. Lett.* **95**, 146802 (2005).
 - [5] B. A. Bernevig and S.-C. Zhang, Quantum spin Hall effect, *Phys. Rev. Lett.* **96**, 106802 (2006).
 - [6] B. Xie, H.-X. Wang, X. Zhang, P. Zhan, J.-H. Jiang, M. Lu, and Y. Chen, Higher-order band topology, *Nat. Rev. Phys.* **3**, 520 (2021).
 - [7] Y. Tokura, K. Yasuda, and A. Tsukazaki, Magnetic topological insulators, *Nat. Rev. Phys.* **1**, 126 (2019).
 - [8] M. Z. Hasan and C. L. Kane, Colloquium: Topological insulators, *Rev. Mod. Phys.* **82**, 3045 (2010).

- [9] X.-L. Qi and S.-C. Zhang, Topological insulators and superconductors, *Rev. Mod. Phys.* **83**, 1057 (2011).
- [10] N. Read and D. Green, Paired states of fermions in two dimensions with breaking of parity and time-reversal symmetries and the fractional quantum Hall effect, *Phys. Rev. B* **61**, 10267 (2000).
- [11] A. Yu. Kitaev, Unpaired Majorana fermions in quantum wires, *Phys.-Usp.* **44**, 131 (2001).
- [12] R. M. Lutchyn, J. D. Sau, and S. Das Sarma, Majorana fermions and a topological phase transition in semiconductor-superconductor heterostructures, *Phys. Rev. Lett.* **105**, 077001 (2010).
- [13] S. Kezilebieke, M. N. Huda, V. Vaňo, M. Aapro, S. C. Ganguli, O. J. Silveira, S. Głodzik, A. S. Foster, T. Ojanen, and P. Liljeroth, Topological superconductivity in a van der Waals heterostructure, *Nature (London)* **588**, 424 (2020).
- [14] S. D. Sarma, M. Freedman, and C. Nayak, Majorana zero modes and topological quantum computation, *npj Quantum Inform.* **1**, 15001 (2015).
- [15] R. M. Lutchyn, E. P. A. M. Bakkers, L. P. Kouwenhoven, P. Krogstrup, C. M. Marcus, and Y. Oreg, Majorana zero modes in superconductor-semiconductor heterostructures, *Nat. Rev. Mater.* **3**, 52 (2018).
- [16] E. Prada, P. San-Jose, M. W. A. de Moor, A. Geresdi, E. J. H. Lee, J. Klinovaja, D. Loss, J. Nygård, R. Aguado, and L. P. Kouwenhoven, From Andreev to Majorana bound states in hybrid superconductor-semiconductor nanowires, *Nat. Rev. Phys.* **2**, 575 (2020).
- [17] D. A. Ivanov, Non-Abelian statistics of half-quantum vortices in p -wave superconductors, *Phys. Rev. Lett.* **86**, 268 (2001).
- [18] A. Stern, Non-Abelian states of matter, *Nature (London)* **464**, 187 (2010).
- [19] C. Nayak, S. H. Simon, A. Stern, M. Freedman, and S. Das Sarma, Non-Abelian anyons and topological quantum computation, *Rev. Mod. Phys.* **80**, 1083 (2008).
- [20] J.-I. Inoue and A. Tanaka, Photoinduced transition between conventional and topological insulators in two-dimensional electronic systems, *Phys. Rev. Lett.* **105**, 017401 (2010).
- [21] N. H. Lindner, G. Refael, and V. Galitski, Floquet topological insulator in semiconductor quantum wells, *Nat. Phys.* **7**, 490 (2011).
- [22] T. Kitagawa, T. Oka, A. Brataas, L. Fu, and E. Demler, Transport properties of nonequilibrium systems under the application of light: Photoinduced quantum Hall insulators without Landau levels, *Phys. Rev. B* **84**, 235108 (2011).
- [23] T. Kitagawa, E. Berg, M. Rudner, and E. Demler, Topological characterization of periodically driven quantum systems, *Phys. Rev. B* **82**, 235114 (2010).
- [24] M. S. Rudner, N. H. Lindner, E. Berg, and M. Levin, Anomalous edge states and the bulk-edge correspondence for periodically driven two-dimensional systems, *Phys. Rev. X* **3**, 031005 (2013).
- [25] L. Jiang, T. Kitagawa, J. Alicea, A. R. Akhmerov, D. Pekker, G. Refael, J. I. Cirac, E. Demler, M. D. Lukin, and P. Zoller, Majorana fermions in equilibrium and in driven cold-atom quantum wires, *Phys. Rev. Lett.* **106**, 220402 (2011).
- [26] F. Nathan and M. S. Rudner, Topological singularities and the general classification of Floquet-Bloch systems, *New J. Phys.* **17**, 125014 (2015).
- [27] S. Yao, Z. Yan, and Z. Wang, Topological invariants of Floquet systems: General formulation, special properties, and Floquet topological defects, *Phys. Rev. B* **96**, 195303 (2017).
- [28] Y. Peng and G. Refael, Floquet second-order topological insulators from nonsymmorphic space-time symmetries, *Phys. Rev. Lett.* **123**, 016806 (2019).
- [29] P. M. Perez-Piskunow, L. E. F. Foa Torres, and G. Usaj, Hierarchy of Floquet gaps and edge states for driven honeycomb lattices, *Phys. Rev. A* **91**, 043625 (2015).
- [30] T. Morimoto, H. C. Po, and A. Vishwanath, Floquet topological phases protected by time glide symmetry, *Phys. Rev. B* **95**, 195155 (2017).
- [31] P. Molignini, W. Chen, and R. Chitra, Generating quantum multicriticality in topological insulators by periodic driving, *Phys. Rev. B* **101**, 165106 (2020).
- [32] T. Kitagawa, M. A. Broome, A. Fedrizzi, M. S. Rudner, E. Berg, I. Kassal, A. Aspuru-Guzik, E. Demler, and A. G. White, Observation of topologically protected bound states in photonic quantum walks, *Nat. Commun.* **3**, 882 (2012).
- [33] M. C. Rechtsman, J. M. Zeuner, Y. Plotnik, Y. Lumer, D. Podolsky, F. Dreisow, S. Nolte, M. Segev, and A. Szameit, Photonic Floquet topological insulators, *Nature (London)* **496**, 196 (2013).
- [34] R.-X. Zhang and S. Das Sarma, Anomalous Floquet chiral topological superconductivity in a topological insulator sandwich structure, *Phys. Rev. Lett.* **127**, 067001 (2021).
- [35] D. T. Liu, J. Shabani, and A. Mitra, Floquet Majorana zero and π modes in planar Josephson junctions, *Phys. Rev. B* **99**, 094303 (2019).
- [36] L.-J. Lang and S. Chen, Majorana fermions in density-modulated p -wave superconducting wires, *Phys. Rev. B* **86**, 205135 (2012).
- [37] P. W. Brouwer, M. Duckheim, A. Romito, and F. von Oppen, Topological superconducting phases in disordered quantum wires with strong spin-orbit coupling, *Phys. Rev. B* **84**, 144526 (2011).
- [38] P. D. Sacramento, Charge and spin edge currents in two-dimensional Floquet topological superconductors, *Phys. Rev. B* **91**, 214518 (2015).
- [39] M. Sato and S. Fujimoto, Topological phases of non-centrosymmetric superconductors: Edge states, Majorana fermions, and non-Abelian statistics, *Phys. Rev. B* **79**, 094504 (2009).
- [40] P. D. Sacramento, M. A. N. Araújo, and E. V. Castro, Hall conductivity as bulk signature of topological transitions in superconductors, *Europhys. Lett.* **105**, 37011 (2014).
- [41] C.-X. Liu and B. Trauzettel, Helical Dirac-Majorana interferometer in a superconductor/topological insulator sandwich structure, *Phys. Rev. B* **83**, 220510(R) (2011).
- [42] T. Oka and H. Aoki, Photovoltaic Hall effect in graphene, *Phys. Rev. B* **79**, 081406(R) (2009).
- [43] T. Mori, Floquet resonant states and validity of the Floquet-Magnus expansion in the periodically driven Friedrichs models, *Phys. Rev. A* **91**, 020101(R) (2015).
- [44] M. Bukov, L. D'Alessio, and A. Polkovnikov, Universal high-frequency behavior of periodically driven systems: from dynamical stabilization to Floquet engineering, *Adv. Phys.* **64**, 139 (2015).
- [45] D. Xiao, M.-C. Chang, and Q. Niu, Berry phase effects on electronic properties, *Rev. Mod. Phys.* **82**, 1959 (2010).

- [46] N. Goldman and J. Dalibard, Periodically driven quantum systems: Effective Hamiltonians and engineered gauge fields, *Phys. Rev. X* **4**, 031027 (2014).
- [47] R. Bott and R. Seeley, Some remarks on the paper of Callias, *Commun. Math. Phys.* **62**, 235 (1978).
- [48] D. Carpentier, P. Delplace, M. Fruchart, and K. Gawędzki, Topological index for periodically driven time-reversal invariant 2D systems, *Phys. Rev. Lett.* **114**, 106806 (2015).
- [49] M. Fruchart, Complex classes of periodically driven topological lattice systems, *Phys. Rev. B* **93**, 115429 (2016).
- [50] J. Yu, R.-X. Zhang, and Z.-D. Song, Dynamical symmetry indicators for Floquet crystals, *Nat. Commun.* **12**, 5985 (2021).
- [51] Y. Pan and B. Wang, Time-crystalline phases and period-doubling oscillations in one-dimensional Floquet topological insulators, *Phys. Rev. Res.* **2**, 043239 (2020).
- [52] R.-L. Chu, J. Shi, and S.-Q. Shen, Surface edge state and half-quantized Hall conductance in topological insulators, *Phys. Rev. B* **84**, 085312 (2011).
- [53] H. Zhang, X. Ma, L. Li, D. Langenberg, C. G. Zeng, and G. X. Miao, Two-step growth of high-quality Nb/(Bi_{0.5}Sb_{0.5})₂Te₃/Nb heterostructures for topological Josephson junctions, *J. Mater. Res.* **33**, 2423 (2018).
- [54] M.-X. Wang, C. Liu, J.-P. Xu, F. Yang, L. Miao, M.-Y. Yao, C. L. Gao, C. Shen, X. Ma, X. Chen, Z.-A. Xu, Y. Liu, S.-C. Zhang, D. Qian, J.-F. Jia, and Q.-K. Xue, The coexistence of superconductivity and topological order in the Bi₂Se₃ thin films, *Science* **336**, 52 (2012).
- [55] Y. Ando, Topological insulator materials, *J. Phys. Soc. Jpn.* **82**, 102001 (2013).
- [56] R. J. Cava, H. Ji, M. K. Fuccillo, Q. D. Gibson, and Y. S. Hor, Crystal structure and chemistry of topological insulators, *J. Mater. Chem. C* **1**, 3176 (2013).
- [57] C.-Z. Chang, J. Zhang, M. Liu, Z. Zhang, X. Feng, K. Li, L.-L. Wang, X. Chen, X. Dai, Z. Fang *et al.*, Thin films of magnetically doped topological insulator with carrier-independent long-range ferromagnetic order, *Adv. Mater.* **25**, 1065 (2013).
- [58] J. Shen, J. Lyu, J. Z. Gao, Y.-M. Xie, C.-Z. Chen, C.-w. Cho, O. Atanov, Z. Chen, K. Liu, Y. J. Hu, K. Y. Yip, S. K. Goh, Q. L. He, L. Pan, K. L. Wang, K. T. Law, and R. Lortz, Spectroscopic fingerprint of chiral Majorana modes at the edge of a quantum anomalous Hall insulator/superconductor heterostructure, *Proc. Natl. Acad. Sci. USA* **117**, 238 (2020).
- [59] M. Kayyalha, D. Xiao, R. Zhang, J. Shin, J. Jiang, F. Wang, Y.-F. Zhao, R. Xiao, L. Zhang, K. M. Fijalkowski, P. Mandal, M. Winnerlein, C. Gould, Q. Li, L. W. Molenkamp, M. H. W. Chan, N. Samarth, and C.-Z. Chang, Absence of evidence for chiral Majorana modes in quantum anomalous Hall-superconductor devices, *Science* **367**, 64 (2020).
- [60] C.-X. Liu, H. J. Zhang, B. Yan, X.-L. Qi, T. Frauenheim, X. Dai, Z. Fang, and S.-C. Zhang, Oscillatory crossover from two-dimensional to three-dimensional topological insulators, *Phys. Rev. B* **81**, 041307(R) (2010).
- [61] J. E. Moore, The birth of topological insulators, *Nature (London)* **464**, 194 (2010).
- [62] X.-L. Qi and S.-C. Zhang, The quantum spin Hall effect and topological insulators, *Phys. Today* **63**(1), 33 (2010).
- [63] A. K. Panda, N. C. Agrawal, R. K. Parida, and G. N. Dash, GaN-based Gunn diode for high frequency signal generation, in *2007 International Workshop on Physics of Semiconductor Devices, Mumbai, India* (IEEE, Piscataway, NJ, 2007), pp. 514–517.
- [64] Q. Yu, Z. Tao, J. Song, Y. C. Tao, and J. Wang, Supercurrent switch in π topological junctions based upon a narrow quantum spin Hall insulator, *Sci. Rep.* **7**, 10723 (2017).
- [65] J. Liao, Y. Ou, H. Liu, K. He, X. Ma, Q.-K. Xue, and Y. Li, Enhanced electron dephasing in three-dimensional topological insulators, *Nat. Commun.* **8**, 16071 (2017).
- [66] D. D. Vu, R.-X. Zhang, Z.-C. Yang, and S. Das Sarma, Superconductors with anomalous Floquet higher-order topology, *Phys. Rev. B* **104**, L140502 (2021).
- [67] D. Vu, Dynamic bulk-boundary correspondence for anomalous Floquet topology, *Phys. Rev. B* **105**, 064304 (2022).
- [68] R.-X. Zhang and Z.-C. Yang, Theory of anomalous Floquet higher-order topology: Classification, characterization, and bulk-boundary correspondence, [arXiv:2010.07945](https://arxiv.org/abs/2010.07945).
- [69] Z. Yan, F. Song, and Z. Wang, Majorana corner modes in a high-temperature platform, *Phys. Rev. Lett.* **121**, 096803 (2018).
- [70] Y.-J. Wu, J. Hou, Y.-M. Li, X.-W. Luo, X. Shi, and C. Zhang, In-plane Zeeman-field-induced Majorana corner and hinge modes in an *s*-wave superconductor heterostructure, *Phys. Rev. Lett.* **124**, 227001 (2020).
- [71] Z. Yan, Majorana corner and hinge modes in second-order topological insulator/superconductor heterostructures, *Phys. Rev. B* **100**, 205406 (2019).
- [72] A. K. Ghosh, T. Nag, and A. Saha, Floquet generation of a second-order topological superconductor, *Phys. Rev. B* **103**, 045424 (2021).
- [73] A. K. Ghosh, T. Nag, and A. Saha, Floquet second order topological superconductor based on unconventional pairing, *Phys. Rev. B* **103**, 085413 (2021).